Modification of the Gallium-Doped Zinc Oxide Surface with Self-Assembled Monolayers of Phosphonic Acids: A Joint Theoretical and Experimental Study

Hong Li, Erin L. Ratcliff, Ajaya K. Sigdel, Anthony J. Giordano, Seth R. Marder, Joseph J. Berry, and Jean-Luc Brédas**

Gallium-doped zinc oxide (GZO) surfaces, both bare and modified with chemisorbed phosphonic acid (PA) molecules, are studied using a combination of density functional theory calculations and ultraviolet and X-ray photoelectron spectroscopy measurements. Excellent agreement between theory and experiment is obtained, which leads to an understanding of: i) the core-level binding energy shifts of the various oxygen atoms belonging to different surface sites and to the phosphonic acid molecules; ii) the GZO work-function change upon surface modification, and; iii) the energy level alignments of the frontier molecular orbitals of the PA molecules with respect to the valence band edge and Fermi level of the GZO surface. Importantly, both density of states calculations and experimental measurements of the valence band features demonstrate an increase in the density of states and changes in the characteristics of the valence band edge of GZO upon deposition of the phosphonic acid molecules. The new valence band features are associated with contributions from surface oxygen atoms near a defect site on the oxide surface and from the highest occupied molecular orbitals of the phosphonic acid molecules.

1. Introduction

N-type transparent conducting oxides (TCOs) have found wide spread applications in organic optoelectronic devices such as light-emitting diodes (OLEDs) or solar cells, either as electrodes or as electron-selective interlayers. Among TCOs, indium tin oxide (ITO) is the most commonly used electrode material due to its low resistivity (on the order of 10^{-4} ~ 10^{-5} Ω cm) and good optical transparency.[1] However, the high cost and limited supply of indium have led to the development of alternative TCO materials over the past ten years, such as fluorine-doped tin oxide (FTO), zinc oxide (ZnO), or indium-, gallium- or aluminum-doped zinc oxide (In:ZnO/Ga:ZnO/Al:ZnO).[2] Zinc oxide, an inexpensive and abundant binary compound, is a transparent semiconductor with a large band gap (3.3–3.4 eV) but relatively high resistivity (on the order of 10^{-3} Ω cm).[3] Its conductivity can be improved via doping, for instance with gallium; in this case, conductivities close to that of ITO can be found for optimized dopant concentrations.[4–7] In addition, Ga:ZnO (GZO) films can be fabricated at room temperature [8–10] and via solution processing,[11] which makes them suitable for use with flexible substrates for plastic electronic applications.[12]

Incorporation of TCO materials into organic electronic devices often requires control over the surface work function of the TCO prior to formation of the oxide/organic interface. By modulating the work function of the TCO, the rate of charge injection or extraction to/from the subsequent layer can be controlled. Tuning the work function can also lead to control over the width of the charge accumulation or depletion layers in the space charge region of the interface that impact the electric fields near the interface.[13] In organic photovoltaic devices specifically, in the case of non-Fermi level pinning of the interface, the systematic control of work function of the contact can be used to alter the open-circuit voltage, and hence, the net power conversion efficiency of the device.[14–20] However, modulating the work function of conducting oxides can be challenging, as it requires an alteration of the surface chemistry of the oxide, for instance, of the local hydroxyl coverage. Recent work highlighting control of the GZO surface work function used a series of surface pretreatments, which demonstrated a clear correlation between impact on surface composition, work function change, and inner and outer sphere electron-transfer rates in solution.[21] Furthermore, it was found that the work-function was not stable over time (minutes to hours) for many of the

Dr. H. Li, A. J. Giordano, Prof. S. R. Marder, Prof. J.-L. Brédas
School of Chemistry and Biochemistry
and Center for Organic Photonics and Electronics
Georgia Institute of Technology
Atlanta, Georgia 30332-0400, USA
E-mail: jean-luc.bredas@chemistry.gatech.edu
Dr. E. L. Ratcliff
Department of Chemistry & Biochemistry
University of Arizona
Tucson, Arizona 85721-0041, USA
E-mail: ratcliff@email.arizona.edu
Dr. A. K. Sigdel, Dr. J. J. Berry
National Renewable Energy Laboratory
1617 Cole Blvd., Golden, Colorado 80401, USA
Prof. J.-L. Brédas
Department of Chemistry
King Abdulaziz University
Jeddah 21589, Saudi Arabia

DOI: 10.1002/adfm.201303670

pretreatments, which suggests that surface pretreatments are not an ideal approach to control work function of an oxide surface.

Surface modification of inorganic electrode materials by organic molecules forming self-assembled monolayers (SAMs) has been widely considered to tune the surface and interface properties in organic electronics applications.[16,19,22,23] Recently, phosphonic acids (PA) have been used to modify the work function of both ITO and ZnO surfaces over a range greater than 1 eV.[24–33] Electro-absorption spectroscopy experiments on devices where a poly(p-phenylenevinylene) derivative ("super yellow") is used as the active layer, have also shown that the built-in potential (V_{BI}) between the PA-modified ITO surface and the active layer scales linearly with the work function of the PA-modified ITO electrode.[34] In a follow-up work, Ratcliff *et al.* demonstrated that systematic variations of the surface work function of ITO, via a series of phosphonic acid SAMs, cause a linear change in the open-circuit voltage of polymer-fullerene devices.[19]

To explore the impact of phosphonic acids as surface modifiers on TCO materials such as GZO, we have performed a combined experimental and theoretical study on the modification of the GZO (002) surface by a series of five phosphonic acids. These include phenyl phosphonic acid (PPA), pentafluorophenyl phosphonic acid (F_5PPA), benzyl phosphonic acid (BPA), pentafluorobenzyl phosphonic acid (F_5BPA), and (2,6) difluorobenzyl phosphonic acid (oF_2BPA), see **Figure 1**. The GZO (002) surface and the binding geometries of the PA molecules on this surface have been explored at the density functional theory (DFT) level to gain a basic understanding of the surface and interface electronic structures. The electronic properties of the bare and modified GZO surfaces have been investigated using both X-ray and ultraviolet photoelectron spectroscopies. Combining the computational results with the experimental photoelectron spectroscopy data allows us to provide insight into: (i) the origin of the core-level binding energy shifts for the oxygen atoms belonging to different surface sites and to the PA molecules; (ii) the SAM-induced change in GZO work function; and (iii) the energy level alignments of the frontier molecular orbitals of the PA molecules with respect to the valence band edge and Fermi level of the GZO surface.

While points (i) and (ii) have been discussed already in the case of PA-modified ITO and ZnO surfaces in earlier theoretical and experimental studies,[24–26,31,32,35,36] determining the energy-level alignments usually remains very challenging when dealing with organic/inorganic interface systems. It is clear that a correct description of the energy level alignments of the molecular frontier orbitals with respect to the Fermi level or valence/conduction band edge of the electrode or interlayer is critical for understanding the charge injection/collection processes at these interfaces; however, many calculations based on density functional theory tend to present results that are not in good agreement with the experimental results coming, for instance, from photoelectron spectroscopy measurements. In the case of physisorbed organic/organic and metal/organic interfaces, as well as in weakly chemisorbed semiconductor/organic interfaces, the work of Neaton and co-workers[37–40] has demonstrated that good agreement can be reached by corrections at different levels within the GW approximation. Similar observations have also been made by Kronik and co-workers[41] and Zojer and co-workers[42] for weakly chemisorbed silicon/alkyl and Au/anthracene selenolate interfaces. Importantly, we find here that in the case of strongly chemisorbed molecules on metal oxide surfaces such as PA molecules bound on the GZO surfaces, density functional theory at the level of generalized-gradient approximation with on-site Coulomb corrections for both Zn and Ga (GGA+U) provides an excellent description of the energy level alignment of the highest occupied molecular orbitals (HOMOs) of the PA molecules with respect to the valence band maximum (VBM) or the Fermi level of the metal oxide surfaces.

2. Experimental and Computational Methods

2.1. Substrate Fabrication

While there are multiple techniques to fabricate GZO thin films, those examined here were deposited via sputtering onto 50.8 mm × 50.8 mm Corning Eagle 2000 glass substrates. A single composition ceramic oxide sputter target with the molar ratio of 97.5% ZnO; 2.5 % Ga_2O_3 (greater than 99.99% pure, Cerac Inc) was used, with film thicknesses ranging from 300 to 500 nm. GZO films were fabricated using sputtering depositions that superimposed RF at 13.56 MHz (Dressler Cerac RF power generator) and DC magnetron sputtering (Advance energy DC

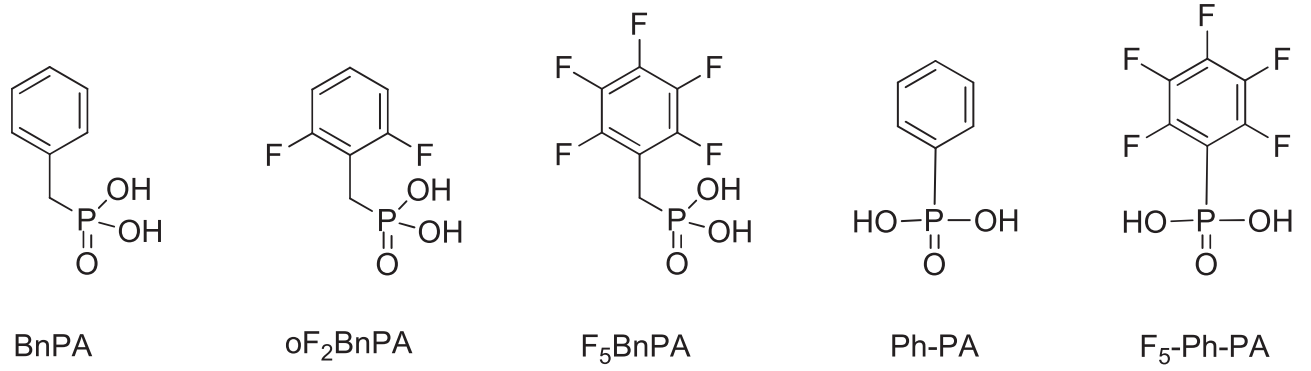

Figure 1. Molecular structures of the PA molecules investigated in this work: benzyl phosphonic acid (BPA), (2,6) difluorobenzyl phosphonic acid (oF_2BPA), pentafluorobenzyl phosphonic acid (F_5BPA), phenyl phosphonic acid (PPA), and pentafluorophenyl phosphonic acid (F_5PPA).

pinnacle plus) with a conventional magnetron sputtering source (Angstrom Sciences, Inc.) in pure argon (>99.999%) atmosphere. These deposition parameters were optimized to obtain films with conductivity of 4500 S/cm,[43] optical transparency of ~90% in the visible wavelength region, and atomic ratios verified by XPS of ~95:5 Zn:Ga prior to any surface pretreatments, which can alter the near-surface composition in Zn and Ga, along with surface adsorbed species. Substrates were oriented parallel to the plane of the target and centered with the racetrack. The films were deposited at a substrate temperature of 250 °C, with a substrate to target distance of 68.5 mm, total power density of ~2.2 W/cm^2, an argon flow into the chamber of 20 sccm, and a total deposition pressure of 0.60 Pa.[44] To facilitate good thermal contact, the substrates were attached with silver paint to the stainless steel heater block and the temperature on the front surface of the substrate was measured in-situ with a physically grounded, unshielded, k-type thermocouple to allow accurate temperature measurements during the deposition. Typically, a temperature rise of approximately 25 °C was observed over the course of a deposition. The chamber base pressure prior to backfilling with argon was less than $<1.3 \times 10^{-4}$ Pa. Each deposition began with a 10-min burn-in period during which the system was allowed to reach steady-state condition before the film deposition was started. After deposition, the substrates were allowed to cool in vacuum until the sample surface temperature was below 100 °C before removal to ambient, in order to minimize strain due to thermal gradient.

2.2. Surface Pretreatments

2.2.1. GZO Surface Preparation

Prior to use, GZO electrodes were cut from the center of the substrate and cleaned in detergent (diluted Triton X-100), followed by rinsing with deionized water. The electrodes were then successively sonicated in acetone for 10 minutes and isopropanol for 5 min, followed by drying in a nitrogen stream. Ideally, a clean surface, free of all carbon, should be used for the bare GZO surface. A carbon-free surface is obtained by argon-ion sputtering at ~2.0×10^{-5} Pa (1.5×10^{-7} Torr) for approximately 5 minutes with an acceleration voltage of 2.0 kV and a sample current of 1.5 μA, which was sufficient time for eliminating any detectable C 1s peak in angle-resolved XPS. However, such a surface is difficult to obtain over a large area and it is not expected that such a surface would remain free of contamination during the adsorption of phosphonic acid modifiers from a solvent. Our recent work demonstrated that an ambient pretreatment of a base rinse resulted in similar surface chemistry and work function as the Ar-ion sputtered surface of the GZO electrode.[21] The "KOH etch" pretreatment etched the electrodes with 6 M aqueous potassium hydroxide solution (Aldrich) for 15 s, followed by rinsing with filtered water and drying in a stream of nitrogen.

2.2.2. Phosphonic Acid Modifications

Immediately following the KOH treatment, samples were immersed in a 10 mM ethanol solution of the phosphonic acid, for 2 h, prior to removal from the ethanol solution. Samples were sonicated in pure ethanol in order to remove any physisorbed molecules, followed by rinsing with ethanol and dried in a nitrogen stream. Cyclic voltammetry of a ferrocene phosphonic acid chemisorbed to the surface yielded a coverage of approximately 1.4×10^{14} molecules/cm^2 (2.4 (±0.3) $\times 10^{-10}$ mol/cm^2) as estimated by the Laviron method; these results are consistent with full monolayer coverage of a carboxylic acid-functionalized ferrocene.[21,45–48]

2.3. XPS/UPS

XPS measurements were performed with a Kratos Axis Ultra X-ray photoelectron spectrometer with a monochromatic Al Kα source at 1486.6 eV and a He(I) excitation source (21.2 eV) for UPS measurements. In the UPS experiments, a –9.00 V bias was applied to the sample to further enhance the collection of the lowest kinetic energy electrons. A separate UPS spectrum was measured for a sputter-etched, atomically clean gold sample before characterization of the GZO electrodes to ensure accurate values for the low and high kinetic edges relative to the Fermi edge. For XPS results, the binding energy calibration of the spectra is corrected following the procedure outlined by Powell, using the Au $4f_{7/2}$ and Cu $2p_{3/2}$ lines, with linearity corrected using the Cu L_3VV line.[49] Prior to each pretreatment, the work function and XPS peaks were measured for the "as received" electrodes, in order to ensure that there were no inconsistencies between samples of GZO that could be misinterpreted to be due to the pretreatments. In each case, the "as received" GZO showed the same results as reported in this work, for both XPS and UPS measurements, within the ±0.1 eV resolution.

2.4. Computational Methodology

The systems studied in this work include both bare and SAM-modified GZO surfaces, with the latter consisting of a layer of two PA molecules per surface unit cell, chemisorbed on the GZO surface. Both the bare and SAM-modified surfaces were evaluated with the repeated-slab approach, with each slab separated by a vacuum space larger than 25 Å. To cancel out spurious dipole–dipole interactions between repeated asymmetric slabs along the surface normal direction, a dipole sheet was introduced in the middle of the vacuum space.

The calculations were carried out at the DFT level with a plane-wave basis set using the Vienna Ab Initio Simulation Package (VASP).[50,51] The semi-local exchange-correlation functional PBE[52] within the generalized gradient approximation and the projector-augmented wave (PAW) method[53] were adopted. A plane-wave cut-off energy of 300 eV for all elements and a total energy convergence of 10^{-6} eV for the self-consistent iterations were used. For the geometry optimizations, only the Γ-point was considered for k-point sampling with the Gaussian smearing method due to the large size of the surface unit cell. For the total-energy calculations, a Γ-centered $2 \times 2 \times 1$ k-point grid was used with the improved tetrahedron method with Blöchl corrections.[54] As detailed in our earlier work on the

modeling of the ZnO surface,[55] the on-site Coulomb interactions among the strongly localized 3d electrons of the Zn and Ga atoms were described by the GGA+U approximation[56] with an effective Hubbard U-parameter (U_{eff} = 8.5 eV) for both Zn-3d and Ga-3d electrons.

We described previously[35] that the work-function change $\Delta\Phi$ of the modified surface can be decomposed into three nearly independent components:

$$\Delta\Phi = \Delta V_{SAM} + \Delta V_{geom.rel.} + \Delta V_{int.dip.} \quad (1)$$

where ΔV_{SAM} is the electrostatic potential energy change across the isolated SAM when it takes the same geometry as in the interfacial system; $\Delta V_{geom.rel.}$ represents the change in work function of the bare slab surface due to geometry relaxation upon deposition of the SAM; and $\Delta V_{int.dip.}$ denotes the potential energy step induced by the charge redistribution at the very interface, related to the formation of an interface bond dipole. The first two terms can be extracted directly from DFT calculations on isolated fragments (SAM and bare slab, both at the geometries adopted in the interfacial system); the latter is obtained by solving Poisson's equation for the plane-averaged electron-density difference $\Delta\rho(z)$ between the combined interface and the isolated fragments, along the surface normal direction z:

$$\frac{d^2V(z)}{dz^2} = -\frac{1}{\varepsilon_0}\Delta\rho(z) \quad (2a)$$

$$\Delta\rho(z) = \rho_{SAM-GZO}(z) - \left[\rho_{GZO}(z) + \rho_{SAM}(z) - \rho_{H1}(z) - \rho_{H2}(z) - \rho_{H3}(z) - \rho_{H4}(z)\right] \quad (2b)$$

where $V(z)$ is the $\Delta\rho(z)$-induced electrostatic potential energy; the terms on the right hand side of Equation (2b) represent, respectively, the plane-averaged electron density of the combined SAM-GZO interface, the bare GZO at the modified geometry, the isolated SAM consisting of two PA molecules per surface unit cell (with the four hydrogen atoms removed upon surface binding being reattached), and the four isolated hydrogen atoms at the same positions as in the SAM.

3. Results and Discussion

3.1. Characterization of Unmodified and PA-modified GZO(002) Surface via DFT Calculations and XPS Experiments

3.1.1. GZO Surface Model

In the theoretical modeling, we consider a Ga doping ratio of ~1.5% (Ga substitutions in a ZnO lattice), which is within the experimentally realized doping ratios of 1–5% for GZO thin films. Recent XPS data for the KOH etched-GZO surface indicates a surface gallium concentration of 2% (surface atomic ratio from XPS) and a statistically similar surface chemistry profile as for Ar-sputtered films.[21] The GZO bulk crystal is first modeled by an orthohombic supercell containing 1 Ga, 63 Zn, and 64 O atoms, with lattice parameters a = 13.0004 Å, b = 11.2587 Å, c = 10.4142 Å, along the [1,1,0], [1,–1,0], and [001] directions, respectively. The supercell lattice parameters are derived from the experimental primitive lattice parameters for the undoped wurtzite ZnO crystal (a = 3.2501 Å, c = 5.2071 Å).[57]

A slab structure modeling the fully-hydroxylated (1/2 OH group per Zn/Ga atom) GZO(002) surface with an intrinsic surface defect consisting of a pair of zinc and oxygen vacancies, has been built based on the optimized crystal structure. The reason for considering such defect pairs comes from the fact that the O 1s XPS spectrum (see below) shows a component at ~2 eV higher binding energy than the main peak; in our earlier modeling of the ZnO surface,[55] such a component has been shown to be associated with surface hydroxyl groups filling the oxygen vacancy site in such defect pairs. The slab contains six Zn-O double layers within a surface unit cell (see **Figure 2**) with the same a and b lattice parameters as for the bulk; the c

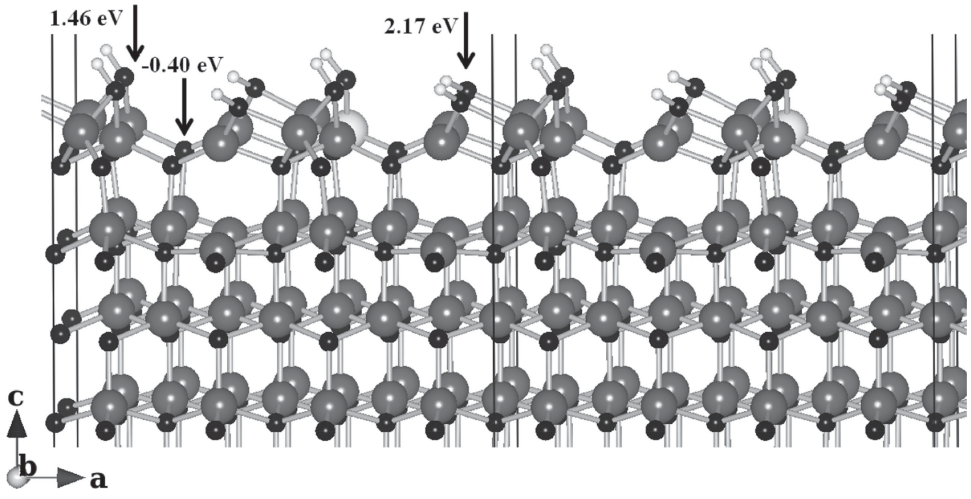

Figure 2. Structure of the hydroxylated GZO(002) surface model containing one Ga atom and one zinc/oxygen vacancy per unit cell. The dark grey, black, light grey, and small white spheres represent Zn, O, Ga, and H, respectively. The DFT-calculated O 1s core-level binding energy shifts for each of the surface oxygen species are given relative to oxygen atoms in the wurtzite GZO crystal, indicated by the values given next to each arrow.

parameter is set to 50 Å, which leads to a vacuum space larger than 25 Å between the repeated slabs. In our earlier work on the ZnO surface, we have compared several nearest-neighbor and non-nearest-neighbor configurations for a pair of zinc and oxygen vacancies (that corresponds to a donor-acceptor pair, or a Schottky defect); it was found that the nearest-neighbor configuration presents a total energy lower by 2.3 eV than that of the non-nearest-neighbor configurations.[55] Here, in order to evaluate the respective locations of both the Ga dopants and the surface defect pair, we have considered both nearest-neighbor and non-nearest-neighbor configurations of a zinc-oxygen vacancy pair located within the top Zn-O double layer and moved the Ga atom within the top three Zn-O double layers in the slab. All Ga, Zn, O, and H atoms within the top four Zn-O double layers are fully geometry relaxed while the bottom two Zn-O double layers remain fixed at their bulk crystal positions. After structural relaxation, the nearest-neighbor configuration has been found to have a lower total energy than the non-nearest-neighbor configuration, by some 1.73 to 0.45 eV as the Ga atom is moved from the top layer to the third layer; this result is consistent with those for the undoped ZnO surface models.[55] Also, placing the Ga atom within the top Zn-O layer provides the energetically most favorable configuration with a total energy 1.73 eV lower than Ga-location in the third Zn-O layer. Therefore, we have chosen as our model structure a GZO(002) surface with a nearest neighbor configuration for the Zn- and O-vacancy pairs and with Ga atoms located within the top Zn-O layer. This is the model surface discussed below.

3.1.2. Adsorption Geometries of Phosphonic Acids on the GZO(002) Surface

The adsorption geometries of the PA molecules are optimized assuming a molecular packing density of 1.3×10^{14} molecules/cm^2 (2.2×10^{-10} mol/cm^2), corresponding to 2 molecules per unit-cell. Such a coverage is consistent with the experimental surface coverage described above ($2.4\ (\pm 0.3) \times 10^{-10}$ mol/cm^2) and can (at least partly) take into account the steric interactions among neighboring molecules. The optimized adsorption geometries of the five PA molecules are shown in **Figure 3**. A tridentate binding mode is obtained for all the molecules, with the PPA and F_5PPA molecules presenting a nearly perpendicular configuration on the GZO surface; the three benzyl PAs display an average tilt angle varying from 56° for the BPA molecule to 65° for F_5BPA (the tilt angle is defined as the angle between the C1-C4 axis of the benzyl ring and the surface normal, see Figure 3). The tilt angle difference (9°) between the non-fluorinated BPA and the fluorinated F_5BPA points to a stronger interaction between the GZO surface and the fluorinated PA molecules, which is associated with the change in charge distribution within the fluorinated benzene rings versus the non-fluorinated ones. This change has been quantified by performing Bader charge analyses on the BPA-GZO and F_5BPA-GZO systems; in the non-fluorinated case, the benzene ring is nearly neutral with a total charge of –0.11|e|, while the ring carries a total positive charge of 3.22 |e| in the fluorinated case. It is also interesting to note that the tilt angle for the BPA molecules on the GZO surface is some 12° larger than the one calculated for tridentate-bound BPA on the undoped stoichiometric ZnO surface (around 44°);[58] this is likely due to the difference in surface electrostatic potential caused by the Ga doping.

The average Zn-O bond length between surface Zn atoms and oxygen atoms belonging to the PO_3 moiety of the benzyl PA molecules (1.89 Å) is some 0.13 Å longer than the Ga-O bond length between a PA molecule and a surface Ga atom. For the phenyl PA molecules, the average Zn-O and Ga-O bond lengths are nearly identical to the benzyl PA instances. Thus, there is no significant difference in the local binding geometries (from PO_3 to the surface Zn or Ga) between the phenyl and benzyl PA molecules despite the large differences in the tilt angles.

3.1.3. O 1s Core-Level Binding Energy Shifts

Based on the theoretical slab model, the relative core-level binding energies of each of the surface oxygen species of GZO and the phosphonic acid modifiers can be evaluated with respect to the binding energy of an oxygen 1s electron in bulk GZO. The shifts in O 1s core-level binding energies are calculated within the final-state approximation as developed by Scheffler and Kresse and implemented in VASP.[59,60] With respect to the bulk oxygens, the core-level binding energy shifts of the oxygen atoms on the GZO surface are calculated to be +2.17 eV for the hydroxyls near an oxygen vacancy, +1.46 eV for the hydroxyls at a bridge site, and -0.40 eV for the oxygen atoms near a zinc vacancy (see Figure 2). For the oxygen atoms within the PO_3 moiety bonded to surface zinc atoms, the calculated average core-level binding energy shifts are +1.07 eV for PPA, +1.24 eV for F_5PPA, +1.09 eV for BPA, and +1.12 eV for both oF_2BPA and F_5BPA. The 0.17 eV difference between PPA and fluorinated F_5PPA is likely due to the short distance between the ortho fluorine atoms and the oxygen atoms of the PO_3 moiety (O2 and O3 in Figure 3(e)), 2.8 Å. In the case of the benzyl PAs, the shortest distance between the fluorine atoms and the oxygen atoms of the PO_3 moiety is 3.3 Å for both the oF_2BPA and F_5BPA molecules; accordingly, the core-level shifts for the two fluorinated benzyl PA molecules are identical and only 0.03 eV larger than the one for the non-fluorinated BPA molecules. Therefore, we expect that the fluorine substituents at the ortho positions would lead to a larger PO_3-related O 1s binding energy shift in the XPS spectra for the phenyl PAs than the benzyl PAs.

3.1.4. XPS Spectra

The XPS spectrum at high surface tilt angle (60°) of the O 1s of the Ar-sputtered GZO electrode is given in **Figure 4**a. The calculated binding energy shifts discussed above have been used to fit the experimental XPS spectra for both bare and PA-modified GZO surfaces with the wurtzite lattice peak set at 530.4 eV. For the bare GZO surface, in addition to the bulk oxygen atoms, three oxygen species have been considered theoretically: (i) surface hydroxyls bridging two surface zinc atoms, referred to as Zn-OH1; (ii) surface hydroxyls at

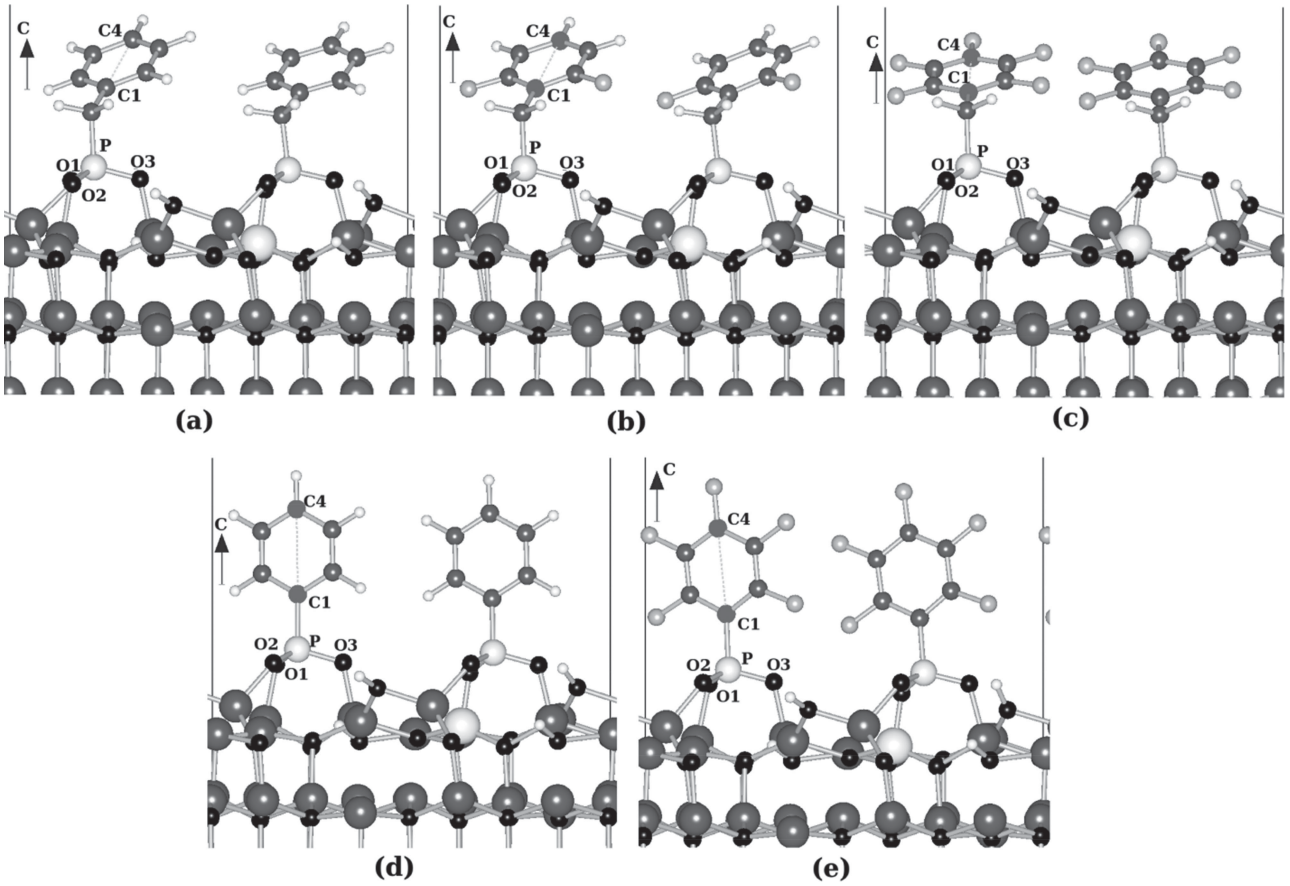

Figure 3. Adsorption geometries of the BPA (a), oF_2BPA (b), F_5BPA (c), PPA (d), and F_5PPA (e) molecules on the GZO surfaces. The black arrow represents the lattice *c* direction (which is coincident with the surface normal direction), and the vertical lines represent the edges of the unit cell. The small dark grey, small light grey, and medium white spheres represent C, F, and P, respectively.

locations near oxygen vacancies (Zn-OH2); and (iii) oxygen atoms near zinc vacancies (O-Zn_V). For the PA-modified GZO surface, an additional oxygen peak is also considered (PO_3-Zn), corresponding to oxygen atoms belonging to the PO_3 moieties. The peak assignments, binding energies, and atomic ratios for the unmodified and modified Ar-sputtered GZO surfaces are given in **Table 1**. The fitting is based on the DFT-calculated relative binding energy shifts, which provides very good agreement with the experimental data (see Figure 4a). There is a higher contribution from the OH group bridging

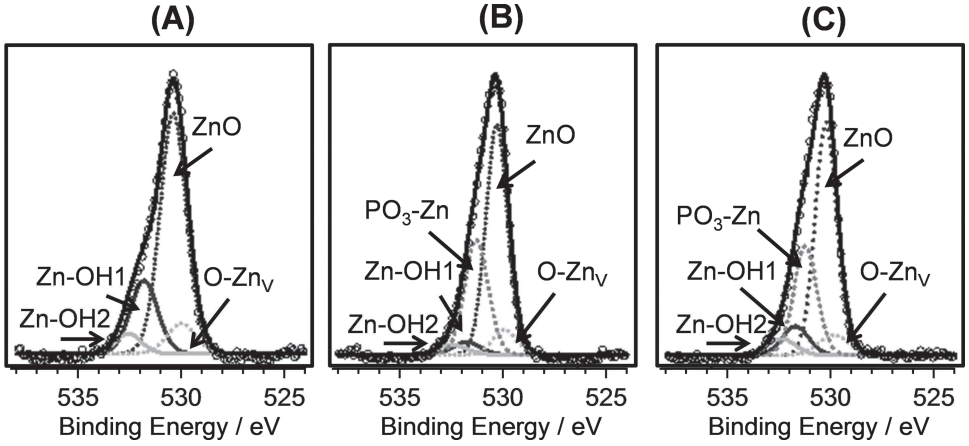

Figure 4. XPS spectra of the O 1s core level fit (total fit given by black lines) using the DFT calculated core-level binding energy shifts (labeled in figure) given in Table 1 for (a) Ar-sputtered GZO; (b) BPA on GZO; and (c) PPA on GZO. The raw data are given by (○) symbols.

Table 1. Peak assignments, binding energies, and atomic ratios for the fits in Figure 4.

	Peak assignment	Binding Energy [eV]	Atomic Ratio [%]
Sputtered GZO	ZnO	530.4	65
	Zn-OH1	531.9	21
	Zn-OH2	532.6	5
	O-Zn_V	530	9
BPA-GZO	ZnO	530.2	53
	Zn-OH1	531.7	8
	Zn-OH2	532.4	5
	O-Zn_V	529.8	7
	PO3-Zn	531.2	27
PhPA-GZO	ZnO	530.2	56
	Zn-OH1	531.7	4
	Zn-OH2	532.4	3
	O-Zn_V	529.8	7
	PO3-Zn	531.2	30

two surface Zn atoms (~21% relative composition) versus hydroxyls near an oxygen-vacancy site (5%). Comparison of the O 1s spectrum with no tilt to the sample (less surface sensitive, not shown) suggests that both sets of hydroxyls are predominantly confined to the surface. Figure 4b and c show high-tilt angle O (1s) spectra for the BPA and PPA modified GZO surfaces, respectively, with corresponding parameters given in Table 1. There is a slightly higher relative composition of phosphorus for PPA vs. BPA, as expected given the smaller molecular footprint of the PPA molecule. The increased spacing between BPA molecules is expected to yield a slightly higher surface hydroxyl coverage for BPA on GZO relative to the PPA modified surface, which is observed in the higher Zn-OH1 (green) and Zn-OH2 (pink) peaks in Figure 4b, relative to Figure 4c. For both modifiers, there is a decrease in the atomic percentage of both the stoichiometric oxide component (ZnO, blue peak) and the OH bridge site between two surface Zn atoms, suggesting the phosphonic acid is binding through these sites.

3.2. Work Function of the GZO(002) Surface Before and After Modification with SAMs

3.2.1. UPS Spectra

The UPS spectra for the sputtered GZO substrate and the five phosphonic acid-modified GZO substrates are shown in **Figure 5**. Work functions are measured as the energetic difference between the Fermi level (E_F) and the vacuum level above the surface, derived from the secondary edge on the left side of the spectra.

For the unmodified GZO surface, the work function is measured to be 3.3 eV, which is consistent with a highly doped ZnO surface and in excellent agreement with the calculated result (3.28 eV, see below). No carbon contamination on the surface is observed with XPS. The onset of the valence band density of states at ~3 eV below the Fermi level, and the corresponding

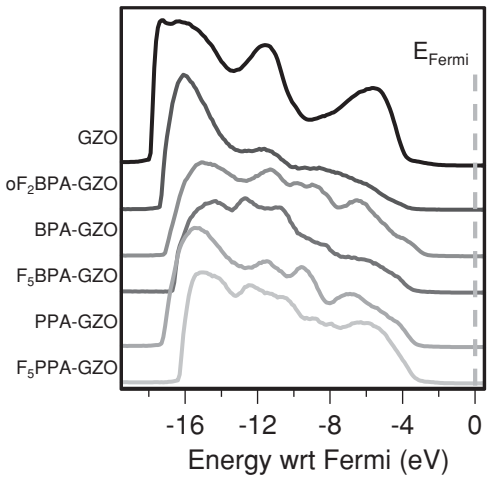

Figure 5. UPS spectra of the sputtered GZO surface (top spectrum) and the phosphonic acid-modified GZO surfaces.

features at 3–5 eV below the Fermi level, are attributed to non-bonding O 2p orbitals, while the states at 5 to 8 eV below the Fermi level have contributions from the O 2p and Zn 4s orbitals.[61] The peak at approximately 12 eV below the Fermi is associated with the filled Zn 3d band.

Modification of the GZO surface with the phosphonic acids shows two distinct changes. The first is a shift in the vacuum level (left side of the spectra) with each of the modifiers. The second one is a change in the valence structure due to contributions from the phosphonic acids, represented by a shoulder near 4 eV below the Fermi level. Specifically, the change in the valence structure is most clear in the non-fluorinated BPA modified surfaces, indicating a dependence on the head group of the surface modifiers.

3.2.2. Work-Function Calculations

The slab surface work function is extracted as the energy difference between the plane-averaged electrostatic potential energy of an electron in the vacuum space above the surface at a distance where the potential energy becomes flat, and the Fermi energy (E_F) of the system. For the GZO(002) surface model, the calculated work function is 3.28 eV.

The calculated and experimental work-function changes for the PA-modified GZO surface are summarized in **Table 2**. Excellent agreement is found between the theoretical results and the experimental values, with the largest difference on the order of ~0.1 eV, which corresponds to the experimental resolution. The PA surface modifiers all increase the work function of the GZO surface, with the largest change [(+1.58 eV (theoretical); 1.57 eV (experimental)] induced by F_5PPA and the smallest change [(+0.42 eV (theoretical); 0.48 eV (experimental)] by oF_2BPA.

3.2.3. Decomposition of the Work-Function Change

The three components contributing to the total work-function changes are given in Table 2. When we compare the

Table 2. DFT-calculated and UPS-measured work function and work-function change for each PA-modified GZO surface, the calculated components contributing to the total work-function change, and the calculated dipole moment of each PA-SAM along the surface normal direction.

	Φ_{cal} [eV]	$\Delta\Phi_{cal}$ [eV]	Φ_{exp} [eV]	$\Delta\Phi_{exp}$ [eV]	ΔV_{SAM} [eV]	$\Delta V_{geom.rel}$ [eV]	$\Delta V_{int.dip.}$ [eV]	$\Delta\Phi_{sum}$ [eV]	μ_z [D]
PPA	3.71	+0.43	3.83	+0.53	–0.23	–0.14	0.78	0.41	0.92
F_5PPA	4.86	+1.58	4.87	+1.57	0.69	–0.25	1.08	1.52	–2.75
BPA	3.91	+0.63	4.03	+0.73	–0.05	–0.13	0.78	0.60	0.21
F_5BPA	4.41	+1.03	4.43	+1.13	0.46	–0.15	0.80	1.11	–1.85
oF_2BPA	3.70	+0.42	3.78	+0.48	–0.32	–0.12	0.84	0.40	1.27

work-function change obtained directly from the DFT slab calculations with the work-function change derived by summing up the three components (ΔV_{SAM} + $\Delta V_{geom.rel.}$ + $\Delta V_{int.dip.}$), the largest difference is about 0.12~0.13 eV, which is typical of what we have found earlier on the ITO and ZnO surfaces [35,58] and confirms the reliability of the decomposition scheme.

Figure 6 shows the correlation between the total work-function change and its components vs. the dipole moment of the PA-SAM layer per surface unit cell (containing two PA molecules) projected along the surface normal, μ_z. Clearly, the variation in total work-function change for the five PA molecules is dominated by the contribution from the molecular SAM (ΔV_{SAM}), which fully correlates with μ_z. This is expected since the binding modes on the surface are nearly identical for all PA molecules. We note that, with the exception of F_5PPA, the $\Delta V_{geom.rel.}$ values are in the range –0.12~0.15 eV and the $\Delta V_{int.dip.}$ values, in the range +0.78 ~ 0.84 eV. In the case of F_5PPA, the corresponding values are -0.25 eV and +1.08 eV, respectively, which points to stronger interactions between these molecules and the surface, as already discussed in Section 3.1.4. Overall, these stronger interactions contribute to further increase the work function by some 0.2 eV.

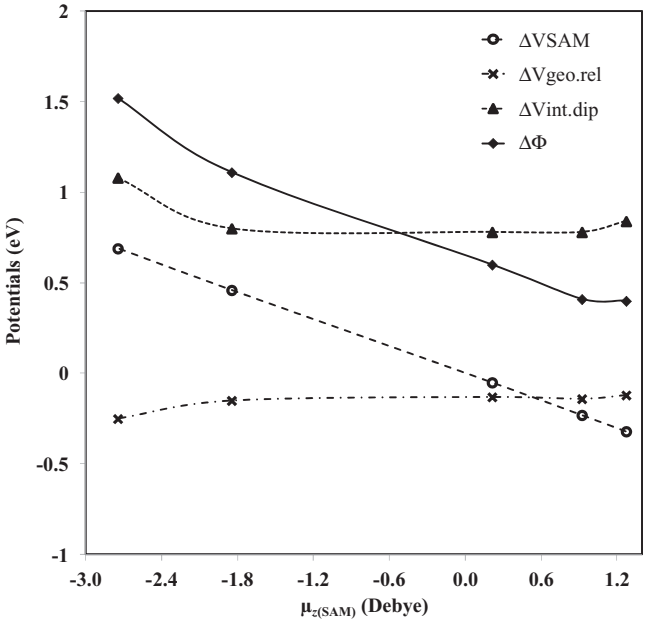

Figure 6. Correlation between the work-function change and its three components and the dipole moment of the molecular SAM along the surface normal (μ_z).

It is also useful to compare the $\Delta V_{geom.rel.}$ and $\Delta V_{int.dip.}$ values for the GZO surface to those obtained at a similar level of theory for the stoichiometric ZnO surface (without charge carriers in the model systems).[58] In such a case, for a tridentate binding of PA surface modifiers, the magnitudes of the two components are much larger, on the order of –0.8 ~ 0.9 eV for $\Delta V_{geom.rel.}$ and +2.1 ~ 2.5 eV for $\Delta V_{int.dip.}$. These results underline the major differences that occur when considering a surface without charge carriers (corresponding to a large-gap intrinsic semiconductor) and a degenerate n-doped surface as we do in the present work.

3.2.4. Charge Transfer at the PA-GZO Interfaces

The plane-averaged electron charge density difference $\Delta\rho$, the total charge difference ΔQ, and the $\Delta V_{int.dip.}$ values obtained by solving Poisson's Equation have been calculated for the five PA modifiers; the results for BPA and F_5PPA are shown in **Figure 7**. In both cases, the $\Delta\rho$ evolution points to a significant charge redistribution within the top part of the slab. The ΔQ evolution is indicative of a small to intermediate amount of electron transfer (~0.15 e for BPA and ~0.33 e for F_5PPA) from the GZO surface to the PA-SAM, mainly localized in the bonding area between the top layer Zn/Ga and the PO_3 moiety. The increased amount of charge transfer in the case of F_5PPA is also consistent with the observation that there exists a stronger interaction between these molecules and the GZO surface.

3.2.5. Energy Level Alignment

The electronic structures of the bare GZO surface and the PA-GZO interface have been analyzed on the basis of calculated densities of states (DOS) and their projections onto different atoms (PDOS). The results for the bare GZO surface and the BPA-GZO interface are given in **Figure 8**. Figure 8a indicates that the Fermi level of the bare GZO slab is located ~0.6 eV above the conduction band minimum (CBM), which underlines that even a very low doping ratio of gallium (Ga:Zn ~ 1.5%) can lead to a degenerately n-doped system. The DOS for the GZO surface shows that the valence band maximum (VBM) lies ~2 eV below the Fermi level; we note that this is some 2 eV higher in energy than the result observed in the UPS measurements (see Figure 5), which is related to the overall underestimation

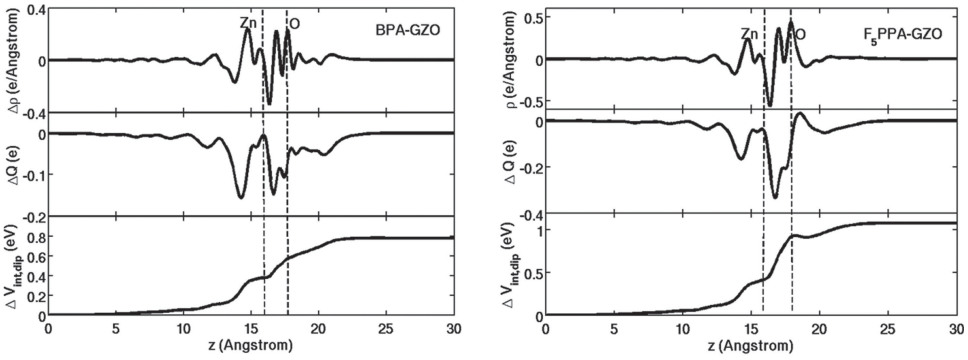

Figure 7. Charge density difference, accumulated charge difference, and the interface dipole for (a) the BPA-GZO and (b) the F_5PPA-GZO interfaces. The two vertical lines describe the average positions of the Zn(Ga) atoms at the top of the GZO surface and of the oxygen atoms of the PO_3 moiety. The z = 0 point is set at the bottom of the supercell, which is 1.45 Å below the bottom layer hydrogen atoms saturating the oxygen dangling bonds.

of the band gaps in DFT-GGA calculations. The DOS for the BPA-GZO interface shows a significant increase in the intensity of the states near the valence band edge upon deposition of the BPA molecules, which are related to the carbon and oxygen atoms of the BPA molecules and the zinc and oxygen atoms of the GZO slab (see inset of Figure 8b). This is further confirmed by the electron charge distribution (Figure 8c) associated with the VBM of the BPA-GZO interface, which corresponds to a combination of the BPA HOMO and contributions from the interface (surface oxygen atoms near a zinc vacancy and bonding of the PO_3 moiety with surface zinc atoms). This is fully consistent with the UPS measurements that display a clear change in the features around the valence band edge (Figure 5) upon surface modification with phosphonic acids.

The DOS and PDOS for the other four PA-GZO interfaces (**Figure 9**) qualitatively show a similar increase in DOS intensity at the VBM. However, in these cases, the intensity increase is less strong and is found to be associated primarily with the interfacial bonding between the PO_3 moiety and the surface zinc atoms; here, the HOMO of the PA molecules (represented by the highest energetic location of the carbon atoms below the E_F, see the insets in Figures 9a–d), is found to distribute in an energy range ~0.2–0.4 eV below the VBM. This can explain the slightly higher valence band edge for the BPA-modified GZO surface observed in the UPS experiments in comparison to the other cases.

Finally, it is important to note the agreement that we obtain here in terms of energy-level alignment between experiment and the GGA-DFT results. This contrasts with the many instances where there occurs an overestimation of the energetic positions of the HOMO and LUMO levels with respect to the Fermi level of metal surfaces, which is attributed to the lack of consideration of surface polarization in standard DFT calculations.[37–42] However, in these cases, the interaction between the organic layer and the surface is either physisorption or weak chemisorption, indicating in general a relatively weak coupling between the organic layer and the surface. Here, there is a strong interfacial bonding between the PO_3 moiety and the surface zinc atoms; this strong coupling appears to dictate the energetic alignment of the frontier molecular orbitals with respect to the VBM of the GZO surface, which is dominated by the contributions from surface oxygen atoms near a zinc vacancy and from surface zinc atoms. Nevertheless, it should also be noted that in weakly coupled metal/organic systems, a

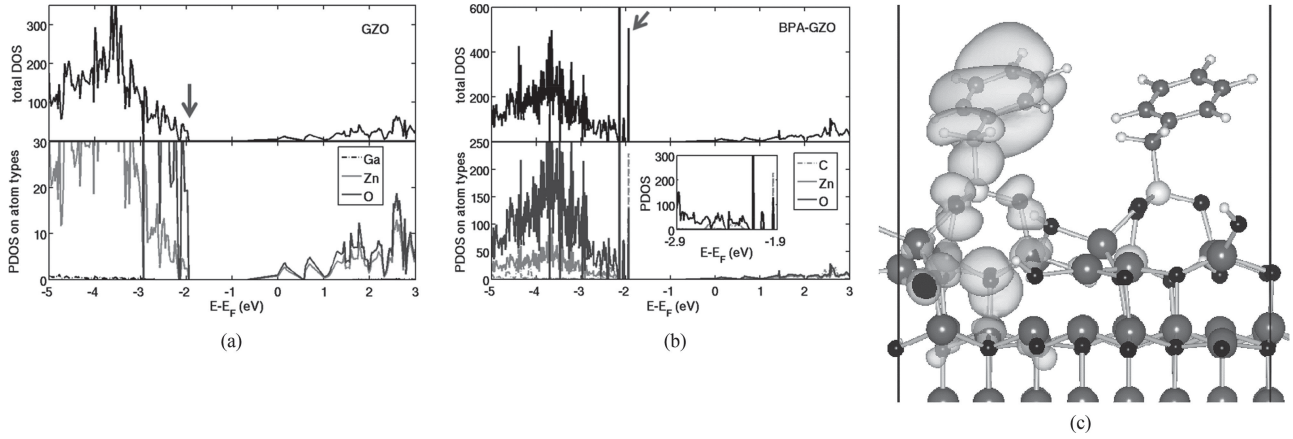

Figure 8. DOS and PDOS for: (a) the bare GZO surface; and (b) the BPA-GZO interface. Panel (c) illustrates the charge distribution corresponding to states associated with BPA HOMO aligned with the VBM of the GZO surface. For clarity, the contribution of zinc atoms is removed in the inset of (b). The black arrows mark the VBM in (a) and (b).

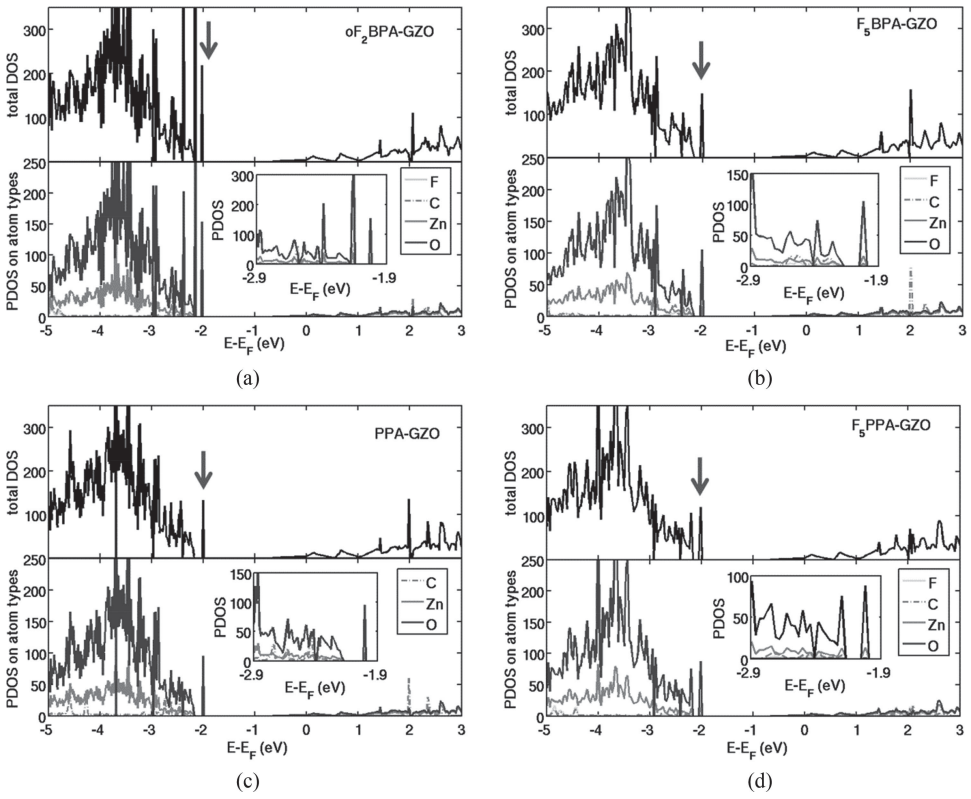

Figure 9. DOS and PDOS for (a) oF$_2$BPA-GZO, (b) F$_5$BPA-GZO, (c) PPA-GZO, and (d) F$_5$PPA-GZO interfaces. The black arrows mark the VBM position.

partial cancellation due to an underestimation of the molecular gap and a lack of consideration of surface polarization could contribute to the calculated energy level alignments.[62] Such effects should be further evaluated for the strongly coupled organic/metal-oxide interfaces studied here.

4. Conclusions

Our combined theoretical and experimental study based on DFT calculations and UPS and XPS measurements, provides a comprehensive understanding of the GZO surface and its interface with phosphonic acid surface modifiers. Excellent agreement between theoretical and experimental results has been obtained regarding the surface work function, the work-function change induced by surface modifications, and the O 1s core-level binding energy shifts for various oxygen species. The experimental and theoretical data both underline a change in the features of the density of states at the valence band edge of GZO upon deposition of PA molecules, associated with contributions from surface oxygen atoms near a zinc vacancy site and the HOMO of the phosphonic acid molecules. The presence of these new interfacial states upon surface modification can impact charge injection or extraction when interfaced with active organic layers, which is critical to improving device performance in organic optoelectronic applications. Similar impact has been observed in recent experimental applications using phosphonic acids as surface modifiers on ITO electrodes.[19,32–34,63]

That a very good agreement is found here between the DFT-calculated energy level alignments and the UPS measurements in terms of the increased intensity of the states near the valence band edge is rather unusual. We attribute it to the strong interfacial bonding between the PA molecules and the GZO surface, which dictates the energy level alignment at such interfaces. It would thus be of interest to investigate other strongly coupled organic/metal-oxide interface systems, such as carboxylic acids chemisorbed on ITO or ZnO surfaces, to evaluate whether a similar agreement is reached regarding the energy level alignment at these interfaces. This would confirm the reliability of standard DFT calculations for energy level alignments at valence band or conduction band edges in the case of strongly coupled organic/metal-oxide interfaces.

Acknowledgements

This work was supported as part of the Center for Interface Science: Solar Electric Materials (CISSEM), an Energy Frontier Research Center funded by the US Department of Energy, Office of Science, Office of Basic Energy Sciences, under Award Number DE-SC0001084 (HL, ELR, AKS, AJG, SRM, JJB, and JLB). The computations reported here were performed mainly at the Georgia Tech Center for Computational Molecular Science and Technology, funded through a NSF CRIF award (Grant No. CHE-0946869) and by the Georgia Institute of Technology.

Received: October 28, 2013
Revised: January 13, 2014
Published online: February 24, 2014

[1] T. Minami, *Semicond. Sci. Tech.* **2005**, *20*, S35.
[2] E. Fortunato, D. Ginley, H. Hosono, D. C. Paine, *MRS Bull.* **2007**, *32*, 242.
[3] H. Cheun, C. Fuentes-Hernandez, J. Shim, Y. Fang, Y. Cai, H. Li, A. K. Sigdel, J. Meyer, J. Maibach, A. Dindar, Y. Zhou, J. J. Berry, J. L. Bredas, A. Kahn, K. H. Sandhage, B. Kippelen, *Adv. Funct. Mater.* **2012**, *22*, 1531.
[4] V. Bhosle, J. Narayan, *J. Appl. Phys.* **2006**, *100*, 093519.
[5] V. Bhosle, A. Tiwari, J. Narayan, *J. Appl. Phys.* **2006**, *100*, 033713.
[6] M. Hiramatsu, K. Imaeda, N. Horio, M. Nawata, *J. Vac. Sci. Technol. A* **1998**, *16*, 669.
[7] B. K. Meyer, J. Sann, D. M. Hofmann, C. Neumann, A. Zenner, *Semicond. Sci. Tech.* **2005**, *20*, S62.
[8] E. M. C. Fortunato, L. M. N. Pereira, P. M. C. Barquinha, A. M. B. do Rego, G. Goncalves, A. Vila, J. R. Morante, R. F. P. Martins, *Appl. Phys. Lett.* **2008**, *92*, 222103.
[9] E. Fortunato, A. Goncalves, V. Assuncao, A. Marques, H. Aguas, L. Pereira, I. Ferreira, R. Martins, *Thin Solid Films* **2003**, *442*, 121.
[10] E. Fortunato, A. Goncalves, A. Marques, A. Viana, H. Aguas, L. Pereira, I. Ferreira, P. Vilarinho, R. Martins, *Surf. Coat. Tech.* **2004**, *180*, 20.
[11] P. K. Nayak, J. Yang, J. Kim, S. Chung, J. Jeong, C. Lee, Y. Hong, *J. Phys. D Appl. Phys.* **2009**, *42*, 035102.
[12] L. A. Wang, J. S. Swensen, E. Polikarpov, D. W. Matson, C. C. Bonham, W. Bennett, D. J. Gaspar, A. B. Padmaperuma, *Org. Electron.* **2010**, *11*, 1555.
[13] M. Fahlman, W. R. Salaneck, *Surf. Sci.* **2002**, *500*, 904.
[14] C. J. Brabec, *Sol. Energ. Mat. Sol. C.* **2004**, *83*, 273.
[15] C. J. Brabec, A. Cravino, D. Meissner, N. S. Sariciftci, T. Fromherz, M. T. Rispens, L. Sanchez, J. C. Hummelen, *Adv. Funct. Mater.* **2001**, *11*, 374.
[16] J. S. Kim, J. H. Park, J. H. Lee, J. Jo, D. Y. Kim, K. Cho, *Appl. Phys. Lett.* **2007**, *91*, 112111.
[17] M. F. Lo, T. W. Ng, T. Z. Liu, V. A. L. Roy, S. L. Lai, M. K. Fung, C. S. Lee, S. T. Lee, *Appl. Phys. Lett.* **2010**, *96*, 113303.
[18] V. D. Mihailetchi, P. W. M. Blom, J. C. Hummelen, M. T. Rispens, *J. Appl. Phys.* **2003**, *94*, 6849.
[19] E. L. Ratcliff, A. Garcia, S. A. Paniagua, S. R. Cowan, A. J. Giordano, D. S. Ginley, S. R. Marder, J. J. Berry, D. C. Olson, *Adv. Energy Mater.* **2013**, *3*, 647.
[20] R. Steim, F. R. Kogler, C. J. Brabec, *J. Mater. Chem.* **2010**, *20*, 2499.
[21] E. L. Ratcliff, A. K. Sigdel, M. R. Macech, K. Nebesny, P. A. Lee, D. S. Ginley, N. R. Armstrong, J. J. Berry, *Thin Solid Films* **2012**, *520*, 5652.
[22] S. Khodabakhsh, B. M. Sanderson, J. Nelson, T. S. Jones, *Adv. Funct. Mater.* **2006**, *16*, 95.
[23] M. Q. Wang, I. G. Hill, *Org. Electron.* **2012**, *13*, 498.
[24] P. J. Hotchkiss, S. C. Jones, S. A. Paniagua, A. Sharma, B. Kippelen, N. R. Armstrong, S. R. Marder, *Accounts Chem. Res.* **2012**, *45*, 337.
[25] P. J. Hotchkiss, H. Li, P. B. Paramonov, S. A. Paniagua, S. C. Jones, N. R. Armstrong, J.-L. Brédas, S. R. Marder, *Adv. Mater.* **2009**, *21*, 4496.
[26] P. J. Hotchkiss, M. Malicki, A. J. Giordano, N. R. Armstrong, S. R. Marder, *J. Mater. Chem.* **2011**, *21*, 3107.
[27] C. L. Perkins, *J. Phys. Chem. C* **2009**, *113*, 18276.
[28] A. Sharma, A. Haldi, P. J. Hotchkiss, S. R. Marder, B. Kippelen, *J. Appl. Phys.* **2009**, *105*, 074511.
[29] A. Sharma, A. Haldi, W. J. Potscavage, P. J. Hotchkiss, S. R. Marder, B. Kippelen, *J. Mater. Chem.* **2009**, *19*, 5298.
[30] A. Sharma, P. J. Hotchkiss, S. R. Marder, B. Kippelen, *J. Appl. Phys.* **2009**, *105*, 084507.
[31] B. B. Zhang, T. Kong, W. Z. Xu, R. G. Su, Y. H. Gao, G. S. Cheng, *Langmuir* **2010**, *26*, 4514.
[32] K. M. Knesting, P. J. Hotchkiss, B. A. MacLeod, S. R. Marder, D. S. Ginger, *Adv. Mater.* **2012**, *24*, 642.
[33] K. M. Knesting, H. X. Ju, C. W. Schlenker, A. J. Giordano, A. Garcia, O. L. Smith, D. C. Olson, S. R. Marder, D. S. Ginger, *J. Phys. Chem. Lett.* **2013**, *4*, 4038.
[34] B. A. MacLeod, N. E. Horwitz, E. L. Ratcliff, J. L. Jenkins, N. R. Armstrong, A. J. Giordano, P. J. Hotchkiss, S. R. Marder, C. T. Campbell, D. S. Ginger, *J. Phys. Chem. Lett.* **2012**, *3*, 1202.
[35] H. Li, P. Paramonov, J. L. Bredas, *J. Mater. Chem.* **2010**, *20*, 2630.
[36] C. Wood, H. Li, P. Winget, J. L. Bredas, *J. Phys. Chem. C* **2012**, *116*, 19125.
[37] J. B. Neaton, M. S. Hybertsen, S. G. Louie, *Phys. Rev. Lett.* **2006**, *97*, 216405.
[38] J. D. Sau, J. B. Neaton, H. J. Choi, S. G. Louie, M. L. Cohen, *Phys. Rev. Lett.* **2008**, *101*, 026804.
[39] I. Tamblyn, P. Darancet, S. Y. Quek, S. A. Bonev, J. B. Neaton, *Phys. Rev. B* **2011**, *84*, 201402.
[40] M. Yu, P. Doak, I. Tamblyn, J. B. Neaton, *J. Phys. Chem. Lett.* **2013**, *4*, 1701.
[41] L. Segev, A. Salomon, A. Natan, D. Cahen, L. Kronik, *Phys. Rev. B* **2006**, *74*, 165323.
[42] A. M. Track, F. Rissner, G. Heimel, L. Romaner, D. Kafer, A. Bashir, G. M. Rangger, O. T. Hofmann, T. Bucko, G. Witte, E. Zojer, *J. Phys. Chem. C* **2010**, *114*, 2677.
[43] A. K. Sigdel, N. E. Widjonako, D. C. Olson, M. T. Lloyd, J. D. Perkins, M. F. A. M. van Hest, S. E. Shaheen, T. Gennett, D. S. Ginley, J. J. Berry, *35th IEEE Phot. Spec. Conf.* **2010**, 3270.
[44] C. W. Gorrie, A. K. Sigdel, J. J. Berry, B. J. Reese, M. F. A. M. van Hest, P. H. Holloway, D. S. Ginley, J. D. Perkins, *Thin Solid Films* **2010**, *519*, 190.
[45] T. J. Gardner, C. D. Frisbie, M. S. Wrighton, *J. Am. Chem. Soc.* **1995**, *117*, 6927.
[46] G. Zotti, G. Schiavon, S. Zecchin, A. Berlin, G. Pagani, *Langmuir* **1998**, *14*, 1728.
[47] A. Berlin, G. Zotti, *Macromol. Rapid Comm.* **2000**, *21*, 301.
[48] C. Carter, M. Brumbach, C. Donley, R. D. Hreha, S. R. Marder, B. Domercq, S. Yoo, B. Kippelen, N. R. Armstrong, *J. Phys. Chem. B* **2006**, *110*, 25191.
[49] C. J. Powell, *Surf. Inter. Anal.* **1995**, *23*, 121.
[50] G. Kresse, J. Furthmuller, *Phys. Rev. B* **1996**, *54*, 11169.
[51] G. Kresse, J. Furthmuller, *Com. Mater. Sci.* **1996**, *6*, 15.
[52] J. P. Perdew, K. Burke, M. Ernzerhof, *Phys. Rev. Lett.* **1996**, *77*, 3865.
[53] P. E. Blochl, *Phys. Rev. B* **1994**, *50*, 17953.
[54] P. E. Blochl, O. Jepsen, O. K. Andersen, *Phys. Rev. B* **1994**, *49*, 16223.
[55] H. Li, L. K. Schirra, J. Shim, H. Cheun, B. Kippelen, O. L. A. Monti, J. L. Bredas, *Chem. Mater.* **2012**, *24*, 3044.
[56] S. L. Dudarev, G. A. Botton, S. Y. Savrasov, C. J. Humphreys, A. P. Sutton, *Phys. Rev. B* **1998**, *57*, 1505.
[57] E. H. Kisi, M. M. Elcombe, *Acta Crystallogr. C* **1989**, *45*, 1867.
[58] C. Wood, H. Li, Paul Winget, Jean-luc Bredas*J. Phys. Chem. C* **2012**, *116*, 19125.
[59] L. Kohler, G. Kresse, *Phys. Rev. B* **2004**, *70*, 165405.
[60] E. Pehlke, M. Scheffler, *Phys. Rev. Lett.* **1993**, *71*, 2338.
[61] V. E. C. Henrich, P. A. Cox, The Surface Science of Metal Oxides, Cambridge University Press, Cambridge, UK **1994**.
[62] A. Biller, I. Tamblyn, J. B. Neaton, Leeor Kronik, *J. Chem. Phys.* **2011**, *135*, 164706.
[63] H. Wang, E. D. Gomez, Z. L. Guan, C. Jaye, M. F. Toney, D. A. Fischer, A. Kahn, Y. L. Loo, *J. Phys. Chem. C* **2013**, *117*, 20474.